Pressure Driven Isostructural Phase Transition in InNbO$_4$: In-situ Experimental and Theoretical Investigations

Alka B. Garg[1*], D. Errandonea[2], C. Popescu[3], D. Martinez-García[2], J. Pellicer-Porres[2], P. Rodríguez-Hernández[4], A. Muñoz[4], P. Botella[2], V. Cuenca-Gotor[5], and J. A. Sans[5]

[1]High Pressure and Synchrotron Radiation Physics Division, Bhabha Atomic Research Centre, Mumbai 400085, India

[2]Departamento de Física Aplicada-ICMUV, MALTA Consolider Team, Universidad de Valencia, Edificio de Investigación, C/Dr. Moliner 50, Burjassot, Valencia 46100, Spain

[3]CELLS-ALBA Synchrotron Light Facility, 08290 Cerdanyola, Barcelona, Spain

[4]Departamento de Física, Instituto de Materiales y Nanotecnología, MALTA Consolider Team, Universidad de La Laguna, La Laguna, E-38205 Tenerife, Spain

[5]Instituto de Diseño para la Fabricación y Producción Automatizada, MALTA Consolider Team, Universitat Politècnica de Valencia, 46022 Valencia, Spain

*Corresponding author
Email: alkagarg@barc.gov.in

Key words: wolframite, InNbO$_4$, x-ray diffraction, Raman spectroscopy, high pressure, phase transition, equation of state

Abstract

The high-pressure behaviour of the technologically important visible-light photocatalytic semiconductor $InNbO_4$, adopting a monoclinic wolframite-type structure at ambient conditions, has been investigated using synchrotron based x-ray diffraction, Raman spectroscopic measurements, and first-principles calculations. The experimental results indicate the occurrence of a pressure induced isostructural phase transition in the studied compound beyond 10.8 GPa. The large volume collapse associated to the phase transition and the coexistence of two phases observed over a wide range of pressure shows the nature of transition to be first order. There is an increase in oxygen anion coordination number around In and Nb cation from six to eight at the phase transition. The ambient-pressure phase has been recovered on pressure release. The experimental pressure-volume data when fitted to a 3rd order Birch-Murnaghan equation of states yields the value of ambient pressure bulk moduli as 179 (2) and 232(4) GPa for the low- and high-pressure phases, respectively. The pressure dependence of the Raman mode frequencies and Gruneisen parameters has been determined for both phases by experimental and theoretical methods. The same information is obtained for the infrared modes from first-principles calculations. Results from theoretical calculations corroborate the experimental findings. They also provide information on the compressibility of interatomic bonds, which is correlated with the macroscopic properties of $InNbO_4$.

Introduction

Indium orthoniobate, $InNbO_4$, belongs to the large family of ABO_4 metal oxides. Depending on the charge and size of the cations, the major structure types adopted by most of the compounds belonging to this series of oxides are zircon, scheelite, monazite, and wolframite [1]. There exist large numbers of experimental and theoretical research articles on these compounds due to their interesting physical properties. Many of these compounds specially materials with V, Nb, and Ta (VB column), and Mo and W (VIB column) at the B site have attracted the attention of many researchers due to their potential applications as scintillators, thermophosphors, photocatalysts, and laser-host materials. Indeed some of them are routinely being used in the industry [2-5]. Apart from various studies at ambient pressure and low temperature [6-7], researchers have investigated in the recent past the high-pressure (HP) behaviour of these materials due to the important role played by compression in altering the physical properties of materials without changing the composition. Combination of x-ray diffraction (XRD), Raman spectroscopic measurements and *ab-initio* calculations on zircon-type ABO_4 rare-earth orthovanadates have established beyond doubt that under high-pressure, these compounds transform from zircon to scheelite to monoclinic M-fergusonite (SG: $C2/c$; No. 15, $Z = 4$) or monoclinic monazite structure. While scheelite and monazite phases obtained under pressure are metastable, the fergusonite phase back transforms to the scheelite phase on pressure release [8-18]. However very recently we have shown that compressing zircon structured $ScVO_4$ non-hydrostatically leads to the fergusonite phase to be metastable [19]. The behaviour of scheelite structured ABO_4 alkaline-earth molybdates and tungstates under compression have also been well documented [20-25]. In contrast with the zircon and scheelite structured materials, much less information is available about the pressure effects on the ABO_4 compounds adopting wolframite and orthorhombic structures [26-28].

Semiconductor ceramics with indium at the A site and V, Nb and Ta at the B site ($InVO_4$, $InNbO_4$ and $InTaO_4$), belonging to ABO_4-type family of compounds, have been reported to show an excellent photocatalytic behaviour, splitting H_2 from pure water under visible light irradiation, indicating their importance in green energy technologies [29]. Errandonea *et al.* have investigated $InVO_4$ and $InTaO_4$ under compression using x-ray diffraction, Raman spectroscopic and optical-absorption techniques along with *ab-initio* calculations. Both compounds show interesting structural and electronic changes at high pressures, with an increase in coordination number around the vanadium and tantalum atoms [30, 31]. To the best of our knowledge, $InNbO_4$ has not yet been investigated under pressure. Since the ionic radii of Nb^{+5} is almost the same as that of Ta^{+5}, both the compounds are isostructural, crystallizing in the wolframite (monoclinic) structure at ambient pressure (space group no. 13, *P2/c*, *Z* = 2) with two kinds of octahedron *viz.* $Nb(Ta)O_6$ and InO_6. These octahedra form separate infinite edge-sharing "zigzag" chains that run along the *c* direction. The InO_6 chains are connected through $Nb(Ta)O_6$ octahedral units to form the three-dimensional network (see figure 1). The volume of InO_6 unit is almost same for both the niobate and tantalate compounds however, slight expansion of TaO_6 in $InTaO_4$ leads to the larger lattice parameters [32]. In the present work, we will report combined experimental and theoretical investigations on $InNbO_4$ under compression at room temperature and the results will be compared with earlier reported findings on $InTaO_4$. Synchrotron based angle dispersive x-ray diffraction (AD-XRD) and Raman spectroscopic measurements have been carried out up to 20.7 and 19.4 GPa respectively. First-principles calculations have also been performed. We will report an accurate determination of equation of state along with characterization and pressure evolution of various vibrational modes for low pressure (LP) and high-pressure (HP) phases for $InNbO_4$. Experimental results are well corroborated with theoretical findings. Evidence of a first-order phase transition beyond 10.8 GPa to another

4

monoclinic structure, which can be described with the same space group (*P2/c*) as the low pressure phase are also reported. The experimental and theoretical evolution of unit-cell parameters and Raman modes for both LP and HP phases are presented. The combined results from experiments and theory would help us in understanding the behaviour of other ternary oxides with wolframite structure under compression.

Experimental Details

Polycrystalline $InNbO_4$ was synthesized by a solid-state reaction method starting from pre-dried In_2O_3 and Nb_2O_5 (purity >99.9%). Both binary oxides were weighed in stoichiometric (1:1) ratio, thoroughly ground in a pestle and mortar, compacted by cold pressing into cylinders of 12.5 mm in diameter and 5 mm in height, and fired at 1200 °C for 24 hrs in a box type programmable resistive furnace. The purity of the synthesized material was confirmed by energy-dispersive x-ray spectroscopy carried out with a transmission electron microscope operated at 200 KeV at the Servei Central de Support a la Investigacio Experimental (SC-SIE) from Universitat de Valencia. Laboratory based powder x-ray diffraction using a rotating-anode generator (RAG) with a Mo (λ = 0.7107 Å) anode and a MAR345 area detector confirmed the single phase formation of the compound with a wolframite-type structure (*P2/c*). The unit-cell parameters obtained at ambient conditions are a = 4.8431(4) Å, b = 5.7709(5) Å, c = 5.1492(5) Å, and β = 91.14(3)$^{\circ}$, in very good agreement with the reported values in the literature [32].

HP-XRD measurements were carried out using a membrane diamond-anvil cell (DAC) equipped with diamonds, having flat culet diameter of 400 μm. A tungsten metal gasket with a central hole of 100 μm, pre-indented to a thickness of 50 μm served as sample chamber. A mixture of methanol-ethanol-water in 16:3:1 ratio served as pressure-transmitting medium. A few fine (1-2 μm diameter) ruby balls were loaded in the sample chamber along with sample for in-situ pressure calibration by ruby fluorescence technique [33]. For XRD

measurements a few fine Cu grains were also loaded with the sample which served as second pressure calibrant [34]. Special care was taken while loading the sample in the hole of gasket to avoid sample bridging between diamonds, which may result in large pressure gradients in the sample [12, 35, 36]. The MSPD-BL04 beamline of the ALBA synchrotron source was used for collecting the HP-XRD data with a monochromatic beam with λ = 0.4246 Å which was focused to a 15×15 μm^2 spot (full-width at half maximum) using Kirkpatrick-Baez mirrors. Two experimental runs were carried out with a maximum pressure achieved of 14.5 and 20.7 GPa in run 1 and run 2, respectively. At each pressure point, minimum two data sets were collected. In one set of the data, x-ray beam was mainly focussed on the sample (used to determine the crystal structure) and in the other set it was focussed primarily on copper grain (used to determine pressure) but it also interacted with the sample. The pressure was determined with an accuracy of 0.1 GPa using the equation of state (EOS) of Cu [34]. Diffraction images were collected using a Rayonix charge-coupled device (CCD) detector with an exposure time of 10–30 seconds. The sample to detector distance along with detector orientation parameters was refined using a CeO_2 diffraction pattern and the FIT2D software [37]. The same software was used to collapse the two-dimensional diffraction images to standard one-dimensional intensity versus 2θ plots. The structural refinement and further data analysis was performed with GSAS software package [38]. In a typical refinement first the background of the XRD pattern was fitted with a Chebyshev polynomial function of first kind with six to eight coefficients. In the second step, the shape of Bragg peaks was modelled using a pseudo-Voigt function. The overall displacement factor (B) and site occupancy factor (SOF) were constrained for all atoms to SOF = 1 and B = 0.025 $Å^2$. This approach was implemented to reduce the number of free parameters used in the refinements and usually found to work well for HP-XRD data [39, 40]. In the first step, only the unit-cell parameters were refined by means of Le-Bail extraction method as implemented in GSAS [38] followed

by the Rietveld refinement of atomic positional parameters by fixing the unit-cell parameters. Finally a full refinement was carried out in which all the crystal-structure parameters were simultaneously refined. A multiphase refinement was carried out for the high-pressure data where two phases coexisted. In such cases, independent peaks were carefully selected to determine the initial values of the relative scale factors. An iterative procedure was then carried out; fitting alternatively the parameters of the different phases until a satisfactory fitting profile and small goodness of fit is reached.

Ambient-pressure and HP Raman spectra were collected in the backscattering geometry using 514.5 nm Ar laser, a Jobin-Yvon TRH1000 spectrometer and thermoelectric-cooled multichannel CCD detector. The setup was calibrated using plasma lines of the argon ion laser. The spectral resolution of the system was < 2 cm^{-1}. The sample loading procedure in high-pressure chamber was same as described above for XRD measurements. For the Raman spectroscopic measurements only the ruby fluorescence technique was used for pressure calibration. A laser power of less than 10 mW before the DAC was used to avoid sample heating.

Theoretical calculation

Total-energy calculations based on density-functional theory (DFT) were carried out using the Vienna *Ab-initio* Simulation Package (VASP) code [41, 42]. We used the generalized-gradient approximation (GGA) [43-45] to consider the exchange-correlation energy and the projected augmented-wave [46] method in order to include the full nodal character of the all electron charge density in the core region. To achieve an accurate description of the properties of InNbO$_4$, due to the presence of oxygen atoms, the basis set of plane waves used in the calculations was extended up to an energy cut-off of 520 eV. In addition, a dense special k-point sampling was used for the Brillouin zone (BZ) integration in order to have well converged energies and forces. The crystal structures considered at

selected volumes were fully relaxed to their optimized configuration through the calculation of forces and stress tensor. In the optimized configurations, the forces on the atoms were less than 0.006 eV/Å and the deviation of the stress tensor from a diagonal hydrostatic form was smaller than 0.1 GPa. The resulting set of energies and volumes (E, V) were fitted with a fourth-order Birch-Murnaghan equation of state (BM-EOS) [47] to evaluate the equilibrium volume (V_0) and determine the pressure (P), bulk modulus (B_0) and its pressure derivative (B_0'). Simulations were performed at zero temperature, and the stable structures and transition pressures were stabilised by analysing the enthalpy-pressure curve. Lattice-dynamics calculations were performed at the zone centre (Γ point) of the BZ to study the optical vibrational modes under pressure. The construction of dynamical matrix at the Γ point of the BZ, employing the direct method, involves separate calculation of the forces in which a fixed displacement from the equilibrium configuration of the atoms within the primitive cell is considered. The frequencies of the normal modes were obtained from the diagonalization of dynamical matrix. The calculations also allow us to identify the symmetry and eigenvectors of vibrational modes at Γ point.

Results and discussion

Figure 2 shows selected powder XRD patterns recorded at various pressures. Diffraction peaks from Cu (pressure marker) and the tungsten gasket (sample chamber) are marked with an asterisk (*) and the hash symbol (#), respectively. All the diffraction peaks from the sample could be assigned to wolframite structure up to 10.8 GPa and no noticeable changes are observed except for the obvious shifting of the Bragg peaks to higher angle due to lattice compression. Figure 3(a) shows a diffraction pattern measured at 1.2 GPa together with the Rietveld refinement assuming the wolframite structure (space group *P2/c*). In the refinement, the atomic positions [In: (2f: 1/2, *y*, 1/4); Nb: (2e: 0, *y*, 1/4); O1: (4g: *x*, *y*, *z*) and O2: (4g: *x*, *y*, *z*)] along with unit-cell parameters, were considered as free parameters. Various

R factors of the refinement and structural parameters obtained at 1.2 GPa are given in table 1. The refined atomic positions at 1.2 GPa are very similar to those obtained at ambient pressure [32]. Similar qualities of refinements were obtained up to 10.8 GPa. Data collected at 11.6 GPa shows the appearance of a few weak peaks around a 2θ value of 6.9, 8.0, and 9.5 degrees indicating a pressure-induced structural instability of the ambient-pressure phase of $InNbO_4$. The next data collected at 12.6 GPa shows an intensity reduction of the peaks coming from the low-pressure (LP) phase while the intensity from the Bragg peaks of the HP phase builds up. This trend continues until 15.2 GPa and the data collected beyond this pressure up to 20.7 GPa, the highest pressure reached in the present investigations, the diffraction peaks from the ambient phase of the sample reduces below the detection limit of the experimental setup and we assume that the diffraction patterns consist of only peaks from the HP phase. A few diffraction patterns collected while releasing the pressure (figure 2) indicates the complete reversibility of the phase transition. In figure 3c the Rietveld refinement of data collected at 0.1 GPa after pressure unloading along with the residual plot is shown. Since $InNbO_4$ is isostructural to $InTaO_4$, the most obvious choice of the structure of the HP phase is similar to the HP phase of $InTaO_4$. As reported earlier, the HP phase of $InTaO_4$ can be described with the same space group as the ambient pressure wolframite ($P2/c$) phase, but the monoclinic beta angle is very close to 90 degree, indicating a pseudo-orthorhombic nature of the crystal structure. Indeed, we could fit all the observed new peaks associated to the HP phase of $InNbO_4$ with the HP wolframite structure as observed for $InTaO_4$. In figure 3b, we show the diffraction pattern along with Rietveld refinement of the data collected at 20.7 GPa. The low values of residuals and small R-factors given in table 1 indicate the goodness of the fit. Similar kinds of refinements were obtained for all the Rietveld refined patterns in the HP phase. For the patterns belonging to HP phase, we could refine the In and Nb positions, however the oxygen positions were not refined due to the average data quality which led to

non-consistent results. Thus, the oxygen positions were fixed to those of the low-pressure wolframite structure at the highest pressure (10.8 GPa). It is worth mentioning here that though both LP and HP phases could be described by same space group, the structural phase transition involves a large volume discontinuity ($\Delta V/V \sim 13\%$) and a coexistence of phases, suggesting the nature of transition to be of first order. There is an increase in coordination number around both In and Nb cation from six to eight in high-pressure phase. However, the mechanism of transition is not well understood and it is beyond the scope of present work, but since the transition is completely reversible on pressure release, the path of bond breaking and remaking (bond reconstruction) may be ruled out. It would be interesting to carry out radial x-ray diffraction studies under high pressure to understand the mechanism of phase transition, as it has been very recently reported by Yue *et al.* [48] for the zircon to scheelite phase transition in $GdVO_4$. The pressure variation of the lattice parameters extracted from the Rietveld refinements for both phases of $InNbO_4$ is plotted in figure 4. A clear anisotropic compressibility is observed in the cell edges, which is typical of most of wolframite-structured compounds [30] and can be correlated with the compression behaviour of various polyhedral units. The lowest compressibility along the chain direction (c-axis) is related to the small variation of the In-In and Nb-Nb distances. The largest compressibility of the b-axis which consists of alternate chains of InO_6 and NbO_6 octahedra is due to the presence of empty space between two kinds of octahedra along (010) direction.

The experimental pressure volume data is plotted in figure 5. In order to make complex trends visible in P–V plot (figure 5), the volume–pressure data were transformed into an f (Eulerian strain) versus F (normalized pressure) plot [49]. For a Birch–Murnaghan EOS the Eulerian strain is given by $f = 0.5[(V_0/V)^{2/3}-1]$ and the normalized stress is defined as $F = p/[3f(1 + 2f)^{5/2}]$. The f–F plot gives a direct indication of the compression behaviour. If the data points lie on a horizontal line of constant F then $B_0' = 4$ and the data can be fitted

with a second-order BM-EOS. If the data lie on an inclined straight line, the data will be adequately described by a third-order BM-EOS. Positive or negative slopes imply $B_0' > 4$ and $B_0' < 4$, respectively. As shown in figure 6a, for the LP phase, the f-F plot clearly shows a positive slop while for the HP phase (figure 6b) the slope is almost zero, indicating that P-V data for high-pressure phase can be fitted with a 2nd order BM-EOS but the low pressure data has to be fitted with 3rd order BM-EOS. Indeed when LP data was fitted 3rd order BM-EOS, the value of B_0' comes out to be 6.8(13) with B_0 as 179(2) GPa. For high-pressure phase, the value of bulk modulus B_0 is 232(4) GPa. The large value of bulk modulus obtained for HP phase is also indicative of the close packing of InO_8 and NbO_8 dodecahedra in HP phase, which can be seen in figure 1. In table 2 we present the various EOS parameters for both phases obtained from experiment and theory (described in the later section of the present manuscript). Note that wolframite $InVO_4$ (B_0=168 GPa) [30] and $InTaO_4$ (B_0=179 GPa) [31] have a similar bulk modulus as wolframite $InNbO_4$ which is consistent with their structural similarity. Bulk modulus of high-pressure wolframite phase for $InNbO_4$ (present results) is also close to that of HP phase of $InTaO_4$ [31].

Figure 7 shows selected Raman spectra of $InNbO_4$ at different pressures up to 19.4 GPa. Group theory analysis predicts a total of eighteen Raman active modes for wolframite structure with point group symmetry (*C2h*), out of which eight are A_g and ten are B_g modes. The observed Raman spectra of $InNbO_4$ resembles with that of other compounds adopting the wolframite structure [50]. The typical spectra consist of two frequency regions. Four Raman bands in high-frequency region (two A_g and two B_g) separated by a phonon gap of nearly 130 cm^{-1} from rest of the Raman modes lying in low frequency region. The Raman mode at the highest frequency of 817 cm^{-1} is the A_g mode involving the motion of O and Nb atoms while the mode with the lowest frequency is a B_g lattice mode which involves the motion of In and Nb atoms. The experimentally determined values of phonon frequencies are compared with

those obtained from lattice dynamic calculations in table 3 with the mode assignment carried out according to the calculations. The agreement between experiment and calculations is good. The relative difference of frequency, R_ω [51] is smaller than 5% for all modes. All the 18 Raman-active modes measured at ambient pressure could be followed up to 11.3 GPa, however the spectra collected at 12.4 GPa, a weak mode appears in the low frequency region. On further increasing the pressure a few more phonons pick up the intensity while the intensity of modes emanating from the LP phase decreases. This behaviour of the pressure evolution of the Raman spectra indicates a pressure-induced phase transition in the material. The phase transition pressure is almost same as observed in x-ray diffraction measurements described in earlier paragraph. Merging of some of the modes was also observed indicating the different pressure coefficients of various frequencies. In the spectra collected at highest pressure of 19.4 GPa, though the most intense peaks are from the HP phase, two modes from the LP phase also could be observed, indicating the large pressure range of phase coexistence. On pressure release, the ambient phase is recovered confirming the observed reversibility of phase transition from x-ray diffraction measurement. The pressure dependence of all the Raman modes can be described with nearly a linear fit as shown in figure 8. The pressure coefficients for each mode ($d\omega/dP$) are tabulated in table 3 together with the Grüneisen parameters $\gamma = (B_0/\omega_0) \times (\partial\omega/\partial P)$. The experimental value of bulk modulus obtained from the present x-ray diffraction data is used to calculate the Grüneisen parameter. As can be seen from the table 3, the slope of all the modes is positive with different numerical values, ruling out the mode softening under pressure. The B_g mode observed at 470 cm^{-1}, which is the only mode corresponding to motion of two oxygen atoms, shows the highest value of Grüneisen parameter, indicating the greater sensitivity of this mode to pressure. A similar behaviour of the equivalent phonon in InTaO$_4$ and in other wolframite-type compounds has been reported earlier [52]. In figure 8 we also show the pressure dependence of Raman modes

corresponding to the HP phase. The frequencies and pressure coefficients are summarized in table 4. Since the HP phase has the same point group symmetry and identical number of atoms per formula unit as the LP wolframite phase, again eight A_g and ten B_g modes are expected. In our experiment, we observed all the eighteen modes. Their wavenumbers are listed in table 4. The mode assignment of all the observed phonons is carried out based on our lattice-dynamic calculations described in the earlier paragraph. Though the number of modes in the LP and HP phases is same, their frequency distribution is quite different. Particularly, the changes are more noticeable in the high-frequency region of the spectrum where the phonon gap is reduced. The redistribution of the high-frequency modes is consistent with the coordination change determined from XRD experiments [53]. The pressure coefficients along with the Grüneisen parameters for HP phase determined from experiment and theory are given in table 4. All the phonons for the HP phase also harden as in the LP phase along with larger values of Grüneisen parameters for most of the phonons lying in low-frequency region which is reverse in the LP phase where the phonons lying at high frequency have the larger Grüneisen parameters. Before we complete the discussion on vibrational behaviour of InNbO$_4$, in figure 9, we show the pressure evolution of calculated IR modes for both LP and HP phases of InNbO$_4$ along with linear fitting to the data. In all, theory predicts fifteen IR-active modes whose wavenumbers along with their pressure coefficients for both the low- and high-pressure phases at ambient pressure and 20.5 GPa, respectively, are given in table 5. Presently there are no experimental reports available in the literature to compare with our calculated frequencies. As can be seen in figure 9, the IR modes have a similar frequency distribution as the Raman modes except the reduction of highest frequency mode to 742 cm^{-1}. In addition, the IR modes show similar sensitivity to pressure as the Raman modes except for the fact that there are three modes with negative pressure coefficients for LP and one phonon for HP phase (table 5).

Now in the following paragraph we will describe the structural details obtained from *ab-initio* calculations. Figure 10 shows the calculated enthalpy-pressure curve. Calculations predict the stability of low-pressure wolframite phase up to 17 GPa and beyond this pressure the HP wolframite phase becomes stable. The calculated structural parameters for both the LP and HP phases are given in table 6. The pressure evolution of the calculated unit-cell parameters including monoclinic angle β for both the phases are plotted in figure 4 along with experimental data showing quite good agreement. Our simulations also provide information on the effect of pressure on atomic positions. Atomic positions at 13.4 GPa are given in table 6 for comparison with the ambient pressure values. We conclude that not only Nb and In atoms moves under compression towards a higher symmetry position, but also the oxygen atoms move considerably. In figure 11 we plot the pressure variation of different bond lengths of In and Nb cation with oxygen anion in the LP and HP phases of $InNbO_4$ along with the volume of coordination polyhedron of In and Nb. The relative change in the volume of InO_6 and NbO_6 octahedra at 10.5 GPa are 6.3% and 3.8%, respectively. This indicates that the NbO_6 units are stiffer then InO_6 units. The bulk modulus of NbO_6 and InO_6 polyhedral units in low-pressure phase comes out to be 258.6(16) and 142.2(7) GPa respectively providing the quantitative information on the compressibility of NbO_6 and InO_6 units. In addition, the distortion index (defined by Bauer [54]) decreases from 0.0208 to 0.0199 for the InO_6 units at 10.5 GPa suggesting octahedral symmetrization under pressure. In case of NbO_6 the distortion index increases from 0.04644 to 0.04741 at 10.5 GPa. The transition involves an increase of the coordination number of In and Nb, from 6 to 8. In the HP phase both the NbO_8 and InO_8 units have a similar compressibility with the value of bulk modulus as 155(4) and 128.5(14) GPa respectively. A final comment needs to be made on the HP phase. The optimization of the HP wolframite structure in the DFT calculations leads to a reduction of the monoclinic structure to an orthorhombic structure in which the β angle is

basically identical to 90°. In the experiments this angle is 90.4°. The optimized orthorhombic structure can be described with space group (*Pcna*), a super-group of space group (*P2/c*). This indicates that the monoclinic structure found in the experiments is a subtle distortion of the structure predicted by calculations. We have checked that the orthorhombic structure cannot explain all the measured Bragg peaks. This can be done only by reducing the symmetry to monoclinic and letting the β angle to be slightly different than 90°. A possible reason for this discrepancy can be the presence of deviatoric stresses, which are not negligible at the experimental conditions where the HP phase is found. In our calculations we have found that a small deviatoric stress of 0.3 GPa would be enough to deform the theoretically predicted orthorhombic structure transforming it into the experimentally observed monoclinic structure.

Summary

$InNbO_4$, a visible light photocatalytic semiconductor compound, has been investigated under high pressure using *in-situ* x-ray diffraction and Raman spectroscopic measurements up to 20.7 and 19.4 GPa, respectively. Results show evidence of first order, isostructural, reversible phase transition beyond 10.8 GPa with nearly 13% volume discontinuity at the transition. The pressure dependence of unit-cell parameters and all Raman modes has been determined for the low- and high-pressure phases. The Grüneisen parameters for all the Raman frequencies are presented. The experimental findings are well corroborated with first-principles calculations. An equation of state for both the phases has been obtained from experiments as well as theory. Ambient pressure bulk modulus for high pressure phase indicates the stiffening of material compared to the ambient wolframite phase. The polyhedral compressibility is also reported. Finally calculations provide information on infrared modes and their behaviour under compression.

References

[1]   Errandonea, D.; Manjón, F. J. *Prog. Mater Sci.* 2008, **53**, 711-773.

[2]   Kolitsch, U.; Holtstam, D. *Eur. J. Mineral.* 2004, **16**, 117-126.

[3]   Mullica, D. F.; Sappenfield, E. L.; Abraham, M. M.; Chakoumakos, B. C.; Boatner, L. A. *Inorg. Chim. Acta* 1996, **248**, 85-88.

[4]   Krankel, C.; Fagundes-Peters, D.; Fredrich, S. T.; Johannsen, J.; Mond, M.; Huber, G.; Bernhagen, M.; Uecker, R. *Appl. Phys. B* 2004, **79**, 543-546.

[5]   Tang, S.; Huang, M.; Wang, J.; Yu, F.; Shang, G.; Wu, J. *J. Alloys Compd.* 2012, **513**, 474-480.

[6]   Smith, S. H.; Wanklyn, B. M. *J. Cryst. Growth* 1974, **21**, 23-28.

[7]   Elliot, R. J.; Harley, R. T.; Hayes, W.; Smith, S. *Proc. R. Soc. A* 1972, **238**, 217-266.

[8]   Mittal, R.; Garg, Alka B.; Vijayakumar, V.; Achary, S. N.; Tyagi, A. K.; Godwal, B. K.; Busetto, E.; Lausi, A.; Chaplot, S. L. *J. Phys.: Condens. Matter* 2008, **20**, 075223-075229.

[9]   Rao, Rekha; Garg, Alka B.; Sakuntala, T.; Achary, S. N.; Tyagi, A. K. *J. Solid State Chemistry* 2009, **182**, 1879-1883.

[10]   Garg, Alka B.; Rao, Rekha; Sakuntala, T.; Wani, B. N.; Vijayakumar, V. *J. Appl. Phys.* 2009, **106**, 063513-063518.

[11]   Garg, Alka B.; Shanavas, K. V.; Wani, B. N.; Sharma, Surinder M. *J. Solid State Chemistry* 2013, **203**, 273-280.

[12]   Garg, Alka B.; Errandonea, D.; Rodríguez-Hernández, P.; López-Moreno, S.; Muñoz, A.; Popescu, C. *J. Phys.: Condens. Matter* 2014, **26**, 265402-265411.

[13]   Garg, Alka B.; Errandonea, D. *J. of Solid State Chemistry* 2015, **226**, 147-153.

[14]   Popescu, C.; Garg, Alka B.; Errandonea, D.; Sans, J. A.; Rodriguez-Hernández, P.; Radescu, S.; Muñoz, A.; Achary, S. N.; Tyagi, A. K. *J. Phys.: Condens. Matter* 2016, **28**, 035402-035411.

[15]   Errandonea, D.; Popescu, C.; Achary, S. N.; Tyagi, A. K.; Bettinelli, M. *Mater. Res. Bull.* 2014, **50**, 279-284.

[16]   Wang, X.; Loa, I.; Syassen, K.; Hanfland, M.; Ferrand, B. *Phys. Rev. B* 2004, **70,** 064109-064114.

[17]   Errandonea, D.; Kumar, R. S.; Achary, S. N.; Tyagi, A. K. *Phys. Rev. B* 2011, **84**, 224121-224128.

[18]   Paszkowicz, W.; Ermakova, O.; Lopez-Solano, J.; Mujica, A.; Muñoz, A.; Minikayev, R.; Lathe, C.; Gierlotka, S.; Nikolaenko, I.; Dabkowska, H. *J. Phys.:   Condens. Matter* 2014, **26**, 025401-025414.

[19]   Garg, Alka B.; Errandonea, D.; Rodríguez-Hernández P.; Muñoz, A. *J. Phys.: Condens. Matter* 2017, **29**, 055401-055412.

[20]   Errandonea, D.; Pellicer-Porres, J.; Manjón, .F J.; Segura, A.; Ferrer-Roca, Ch.; Kumar, R.S.; Tschauner, O.; Rodríguez-Hernández, P.; López-Solano, J.; Radescu, S.; Mujica, A.; Muñoz, A.; Aquilanti, G. *Phys. Rev. B* 2005, **72**, 174106-174119.

[21]   Errandonea, D.; Manjon, F. J. *Prog. Mater. Sci.* 2008, **53**, 711-773 and references therein.

[22]   Zhang, Y.; Holzwarth, N. A. W.; Williams, R. T. *Phys. Rev. B* 1998, **57**, 12738-12750.

[23] Annenkov, A. A.; Korzhik, M. V.; Lecoq, P. *Nucl. Instrum. Methods Phys. Res., Sect. A* 2002, **490**, 30-50.

[24] Nikl, M.; Bohacek, P.; Mihokova, E.; Solovieva, N.; Vedda, A.; Martini, M.; Pazzi, G. P.; Fabeni, P.; Kobayashi, M.; Ishii, M. *J. Appl. Phys.* 2002, **91**, 5041-5044.

[25] Brenier, A.; Jia, G.; Tu, C. *J. Phys.: Condens. Matter* 2004, **16**, 9103-9108.

[26] Ruiz-Fuertes, J.; López-Moreno, S.; López-Solano, J.; Errandonea, D.; Segura, A.; Lacomba-Perales, R.; Muñoz, A.; Radescu, S.; Rodríguez-Hernández, P.; Gospodinov, M.; Nagornaya, L. L.; Tu, C. Y. *Phys. Rev. B* 2012, **86**, 125202-125210.

[27] Ruiz-Fuertes, J.; Segura, A.; Rodríguez, F.; Errandonea, D.; Sanz-Ortiz, M. N. *Phys. Rev. Lett.* 2012, **108**, 166402-166405.

[28] Lacomba-Perales, R.; Errandonea, D.; Martinez-Garcia, D.; Rodríguez-Hernandez, P.; Radescu, S.; Mujica, A.; Muñoz, A.; Chervin, J. C.; Polian, A. *Phys. Rev. B* 2009, **79**, 094105-09414.

[29] Ye, J.; Zou, Z.; Arakawa, H.; Oshikiri, M.; Shimoda, M.; Matsushita, A.; Shishido, T. *J. Photochemistry and Photobiology A* 2002, **148**, 79-83.

[30] Errandonea, D.; Gomis, O.; García-Domene, B.; Pellicer-Porres, J.; Katari, V.; Achary, S. N.; Tyagi, A. K.; Popescu, C. *Inorg. Chem.* 2013, **52**, 12790-12798.

[31] Errandonea, D.; Popescu, C.; Garg, A. B.; Botella, P.; Martinez-Garc´ıa, D.; Pellicer-Porres, J.; Rodr´ıguez-Hern´andez, P.; Munoz, A.; Cuenca-Gotor, V.; Sans, J. A. *Phys. Rev. B* 2016, **93**, 035204-035212.

[32] Liebertz, Von J. *Acta Cryst. B* 1972, **28**, 3100.

[33] Syassen, K., *High Pres. Res.* 2008, **28**, 75–126.

[34] Agnès, D.; Marc, T.; Paul, L.; Mohamed, M. *Phys. Rev. B*   2008, **78**, 104102-104113.

[35] Errandonea, D. *Cryst. Res. Techn.* 2015, **50**, 729–736.

[36] Errandonea, D.; Muñoz, A.; Gonzalez-Platas, J. *J. Appl. Phys.* 2014, **115**, 216101.

[37] Hammersley, A. P.; Svensson, S. O.; Hanfland, M.; Fitch, A. N.; Häusermann, D. *High Pres. Res.*1996, **14**, 235-248.

[38] Larson, A. C.; von Dreele, R. B. *LANL Report* 2004, 86–748.

[39] Abraham, Y.; Holzwarth, N. A. W.; Williams, R. T. *Phys. Rev. B* 2000, **62**, 1733-1741.

[40] Gleissner, J.; Errandonea, D.; Segura, A.; Pellicer-Porres, J.; Hakeem, M. A.; Proctor, J. E.; Raju, S. V.; Kumar, R. S.; Rodrıguez-Hernandez, P.; Munoz, A.; Lopez-Moreno, S.; Bettinelli, M. *Phys. Rev. B* 2016, **94**, 134108-134120.

[41] Kresse, G.; Hafner, J. *Phys. Rev.B* 1993, **47**, 558-561.

[42] Kresse, G.; Furthümller, J. *Phys. Rev.B* 1996, **54**, 11169-11186.

[43] Perdew, J. P.; Burke, K.; Wang, Y. *Phys. Rev. B* 1996, **54**, 16533-16539.

[44] Perdew, J. P.; Burke, K.; Ernzerhof, M. *Phys. Rev. Lett.* 1996, **77**, 3865-3868.

[45] Kresse, G.; Joubert, D. *Phys. Rev .B* 1999, **59**, 1758-1775.

[46] Blöchl, E. *Phys. Rev. B* 1994, **50**, 17953-17979.

[47] Birch, F. *Phys. Rev.* 1947, **71**, 809-824.

[48] Yue, B.; Hong, F.; Merkel, S.; Tan, D.; Yan J.; Chen B.; Mao H. K. *Phys. Rev. Lett.* 2016, **117**, 135701-135706.

[49] R. J. Angel, Equations of state, in: R. M. Hazen and R. T. Downs (Eds.), *High temperature and high-pressure crystal chemistry*. MSA Reviews in Mineralogy and Geochemistry, vol. 41, pp. 35–60 (Mineralogical Society of America, 2000).

[50] Iliev, M. N.; Gospodinov, M. M.; Litvinchuk, A. P. *Phys. Rev. B* 2009, **80**, 212302-212305.

[51] Errandonea, D.; Munoz, A.; Rodriguez-Hernandez, P.; Gomis, O.; Achary, S. N.; Popescu, C.; Patwe, S. J.; Tyagi, A. K. Inorg. Chem. 2016, **55**, 4958−4969.

[52] Ruiz-Fuertes, J.; Errandonea, D.; Gomis, O.; Friedrich, A.; Manjon, F. J. *J. Appl. Phys.* 2014, **115**, 043510-043514.

[53] Errandonea, D.; Manjón, F. J.; Muñoz, A.; Rodríguez-Hernández, P.; Panchal, V.; Achary, S. N.; Tyagi, A. K. *J. Alloys Compd.* 2013, **577**, 327-335.

[54] Baur, W. H. *Acta Crystallogr. B* 1974, **30**, 1195-1215.

Table 1: Structural parameters of LP wolframite InNbO$_4$ at 1.2 GPa (Top), and HP wolframite at 20.7 GPa. Both structures can be described with space group *P2/c*. For the LP(HP) phase, the goodness of fit parameters are: R$_{wp}$ = 1.43 % and R$_P$ = 1.2 % (R$_{wp}$ = 1.1 % and R$_P$ = 1.0 %). The Wyckoff position for each atom is indicated in the first column. For the HP phase only the In and Nb positions have been refined.

$a = 4.83160(28)$ Å, $b = 5.75520(30)$ Å, $c = 5.13269(27)$ Å, $\beta = 91.2151(30)$ ° 1.2 GPa			
Atom	x	y	z
In (2f)	0.5	0.6821(16)	0.25
Nb (2e)	0	0.1775(20)	0.25
O$_1$ (4g)	0.225(4)	0.898(4)	0.422(7)
O$_2$ (4g)	0.260(4)	0.610(5)	0.901(7)
$a = 4.8507(15)$ Å, $b = 5.0793(15)$ Å, $c = 4.8952(13)$ Å, $\beta = 90.457(22)$° 20.7 GPa			
Atom	x	y	z
In (2f)	0.5	0.723(12)	0.25
Nb (2e)	0	0.216(12)	0.25
O$_1$ (4g)	0.213	0.898	0.438
O$_2$ (4g)	0.265	0.617	0.902
$a = 4.8411(8)$ Å, $b = 5.7724(9)$Å, $c = 5.1448(9)$Å, $\beta = 91.139(8)$° 0.1 GPa (released)			
Atom	x	y	z
In (2f)	0.5	0.6979(15)	0.25
Nb (2e)	0	0.1644(18)	0.25
O$_1$ (4g)	0.229(6)	0.934(5)	0.428(8)
O$_2$ (4g)	0.273(8)	0.637(5)	0.926(9)

Table 2: EOS parameters for different structures determined from present experiments and calculations.

Phase	BM-EOS	V_0 (Å^3)	B_0 (GPa)	B_0'
LP	Exp. 2nd order	143.66(5)	194(2)	4
	Exp. 3rd order	143.73(5)	179(2)	6.8(13)
LP	Theo. 2nd order	145.22(10)	157(2)	4
	Theo. 3rd order	145.06(5)	169.2(12)	2.5(5)
HP	Exp. 2nd order	130.26(12)	231(4)	4
	Exp. 3rd order	130.25(12)	232(4)	4.0(4)
HP	Theo. 2nd order	135.18(10)	178.5(18)	4
	Theo. 3rd order	135.19(10)	178.1(18)	4.02(19)

Table 3: Measured and calculated Raman modes at ambient pressure, pressure coefficients, and Grüneisen parameters for the low-pressure phase of InNbO$_4$. R$_\omega$ is the relative difference between measured and calculated frequencies.

Mode	Experiment (B$_0$ = 179 GPa)			Theory (B$_0$ = 169 GPa)			
	ω (cm^{-1})	dω/dP (cm^{-1}/GPa)	γ	ω (cm^{-1})	dω/dP (cm^{-1}/GPa)	γ	R$_\omega$
B$_g$	120	0.57	0.85	115.9	0.32	0.46	3.4
A$_g$	122	0.52	0.76	117.0	0.43	0.62	4.1
B$_g$	151	0.71	0.84	145.3	0.71	0.82	3.8
B$_g$	185	0.56	0.54	177.1	0.34	0.32	4.3
B$_g$	196	0.56	0.51	188.9	0.57	0.51	3.6
A$_g$	243	0.62	0.45	234.7	0.97	0.69	3.4
A$_g$	279	0.52	0.33	265.9	0.38	0.24	4.7
B$_g$	295	1.46	0.88	278.4	1.55	0.94	5.6
B$_g$	331	1.95	1.05	324.1	1.75	0.91	2.1
A$_g$	352	0.90	0.45	337.1	3.15	1.58	4.2
A$_g$	402	1.93	0.86	383.2	1.89	0.83	4.7
B$_g$	410	3.96	1.73	397.2	4.31	1.83	3.1
B$_g$	470	4.96	1.89	455.8	4.40	1.63	3.0
A$_g$	501	4.48	1.60	488.9	3.30	1.14	2.4
B$_g$	633	5.00	1.41	621.1	5.43	1.47	1.9
A$_g$	651	2.98	0.82	641.5	4.71	1.24	1.5
B$_g$	675	3.89	1.03	669.7	5.34	1.34	0.8
A$_g$	817	3.58	0.78	791.6	4.20	0.89	3.1

Table 4: Measured and calculated Raman modes, pressure coefficients, and Grüneisen parameters of high-pressure phase of InNbO$_4$ at 19.4 GPa. R$_\omega$ is the relative difference between measured and calculated frequencies.

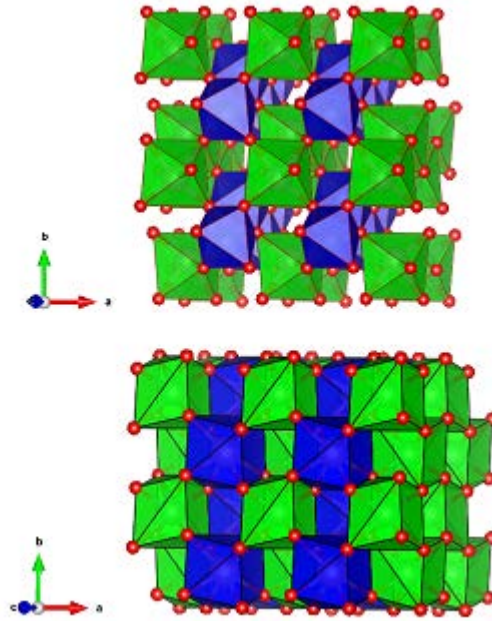|	Experiment (B$_0$ = 232 GPa)			Theory (B$_0$ = 178.1 GPa)			
Mode	ω (cm^{-1})	dω/dP (cm^{-1}/GPa)	γ	ω (cm^{-1})	dω/dP (cm^{-1}/GPa)	γ	R$_\omega$
A$_g$	96	2.97	7.18	88.1	5.25	10.61	8.2
B$_g$	133	1.55	2.70	147.1	1.26	1.52	10.6
B$_g$	160	0.79	1.14	156.3	0.92	1.05	2.3
B$_g$	178	1.26	1.64	168.2	2.82	2.99	5.5
B$_g$	220	1.05	1.11	180.1	2.46	2.43	18.1
A$_g$	233	2.13	2.12	196.7	1.89	1.71	15.5
A$_g$	273	2.21	1.88	203.3	0.38	0.33	25.5
A$_g$	333	1.57	1.09	304.1	1.91	1.12	8.6
B$_g$	357	0.78	0.51	387.7	2.86	1.31	8.6
A$_g$	372	2.77	1.73	395.3	0.57	0.25	6.2
B$_g$	405	3.73	2.14	433.7	1.25	0.51	7.1
B$_g$	466	1.55	0.77	448.6	2.96	1.17	3.7
A$_g$	595	2.11	0.82	520.2	2.43	0.83	12.5
B$_g$	639	1.31	0.47	548.4	1.58	0.51	14.1
B$_g$	702	1.40	0.46	667.3	3.36	0.89	4.9
A$_g$	755	3.92	1.20	726.6	2.41	0.59	3.7
B$_g$	788	2.89	0.85	751.4	2.86	0.67	4.6
A$_g$	850	4.10	1.12	768.4	2.50	0.58	9.6

Table 5: Calculated IR modes and pressure coefficients for the low- and high-pressure phases of $InNbO_4$, at ambient pressure and 20.5 GPa, respectively.

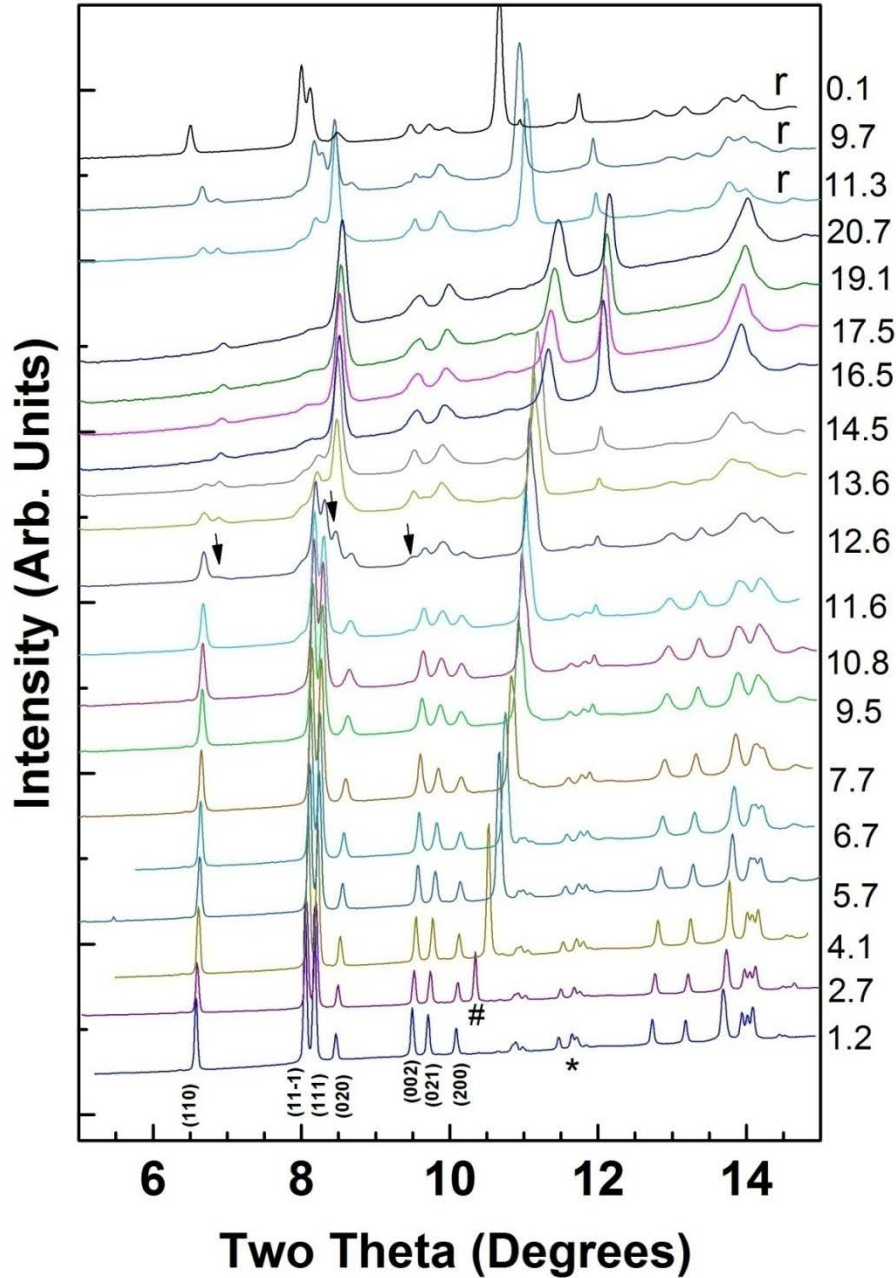|	Low Pressure (B_0 = 169.2 GPa)			High Pressure (B_0 = 178.1 GPa)		
Mode	ω (cm^{-1})	dω/dP	γ	ω (cm^{-1})	dω/dP	γ
B_u	144.7	-1.77	-2.07	94.1	3.92	7.42
A_u	190.2	0.098	0.08	124.8	4.58	6.53
B_u	192.6	0.13	0.11	135.5	3.29	4.32
B_u	217.1	-1.02	-0.79	201.2	1.89	1.67
B_u	266.3	0.02	0.01	202.2	0.42	0.37
A_u	285.7	1.41	0.83	215.4	0.81	0.67
A_u	311.7	-0.30	-0.16	216.4	-1.39	-1.14
B_u	331.4	1.19	0.60	340.9	0.46	0.24
A_u	426.5	3.44	1.36	418.5	2.13	0.91
B_u	455.9	4.47	1.65	505.9	0.83	0.29
B_u	491.5	4.81	1.65	584.1	3.44	1.05
A_u	500.8	4.54	1.53	622.7	3.54	1.01
A_u	572.9	4.98	1.47	623.8	2.40	0.68
B_u	610.5	5.06	1.40	662.9	1.70	0.45
A_u	742.7	3.83	0.87	797.6	2.04	0.45

Table 6: Structural details of wolframite from calculations for $InNbO_4$ at ambient pressure (top), high pressure (bottom) at 20.4 GPa
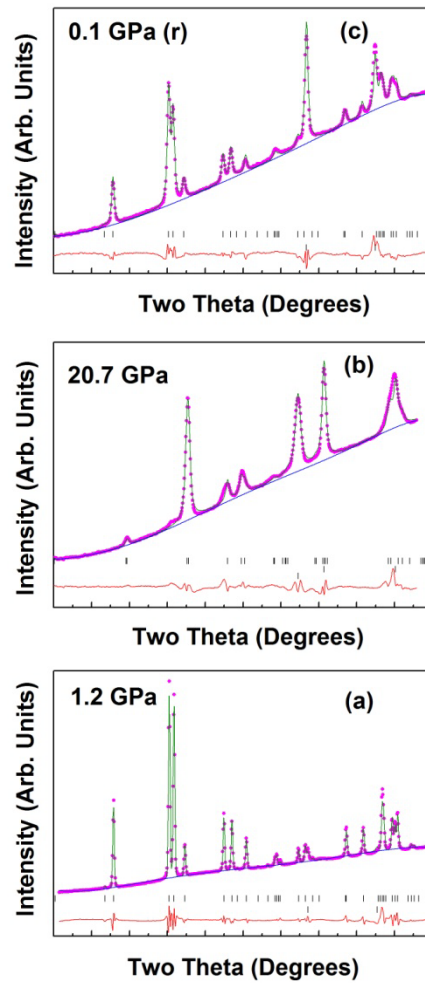
$a = 4.85579$ Å, $b = 5.80105$ Å, $c = 5.14831$ Å, $\beta = 90.9774°$			
Atom	x	y	z
In (2f)	0.5	0.68069	0.25
Nb(2e)	0	0.17676	0.25
O_1 (4g)	0.22420	0.89826	0.42752
O_2 (4g)	0.25970	0.61905	0.90084
$a = 4.92582$ Å, $b = 5.05204$ Å, $c = 4.94265$ Å, $\beta = 90.0014°$			
Atom	x	y	z
In (2f)	0.5	0.75	0.25
Nb (2e)	0	0.24999	0.25
O_1 (4g)	0.24160	0.94580	0.47020
O_2 (4g)	0.25840	0.55415	0.97020

Figure 1: (color online) Crystal structure of low-pressure wolframite (top) and high-pressure wolframite (bottom) phases of InNbO₄. Octhahedral and dodecahedral coordination around In and Nb cations are clearly seen in LP and HP phase respectively.
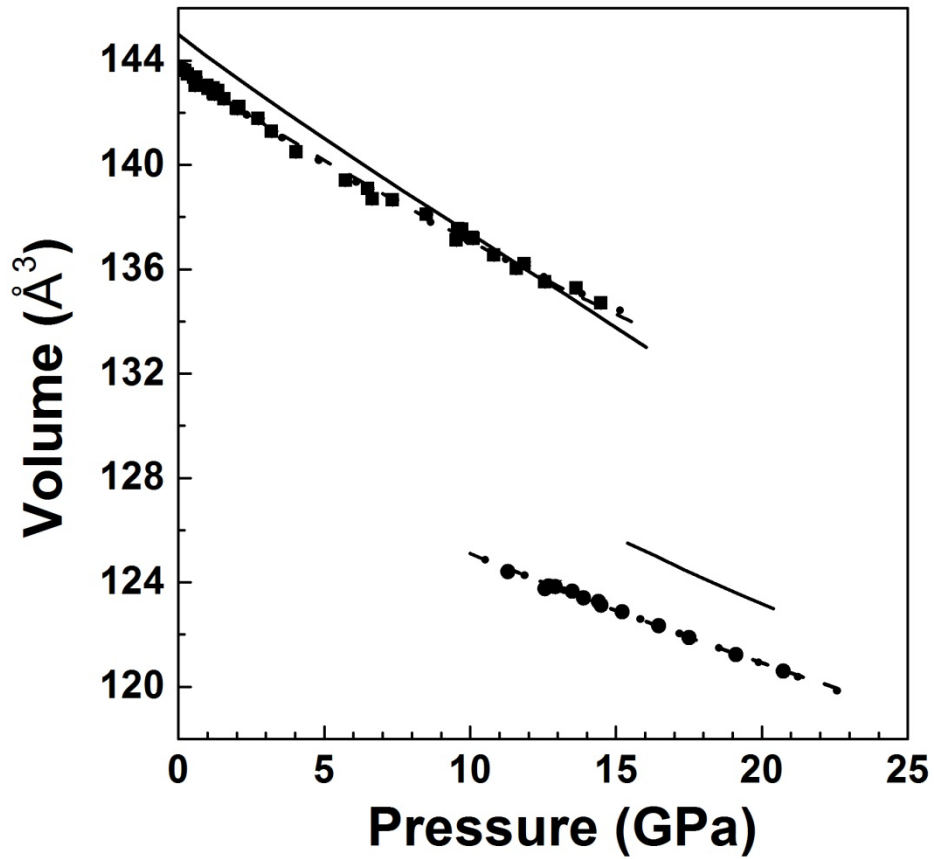
Figure 2: (color online) Pressure evolution of x-ray diffraction patterns of InNbO4. Pressures in GPa, are indicated on the right hand side y-axis. The asterisks denote the peaks from cu pressure marker whereas # indicates the peaks from w sample chamber. The intense peaks from the ambient wolframite structure have been marked. Arrows indicate the appearance of new diffraction peaks from the high pressure phase. Data marked with r were measured during pressure unloading.
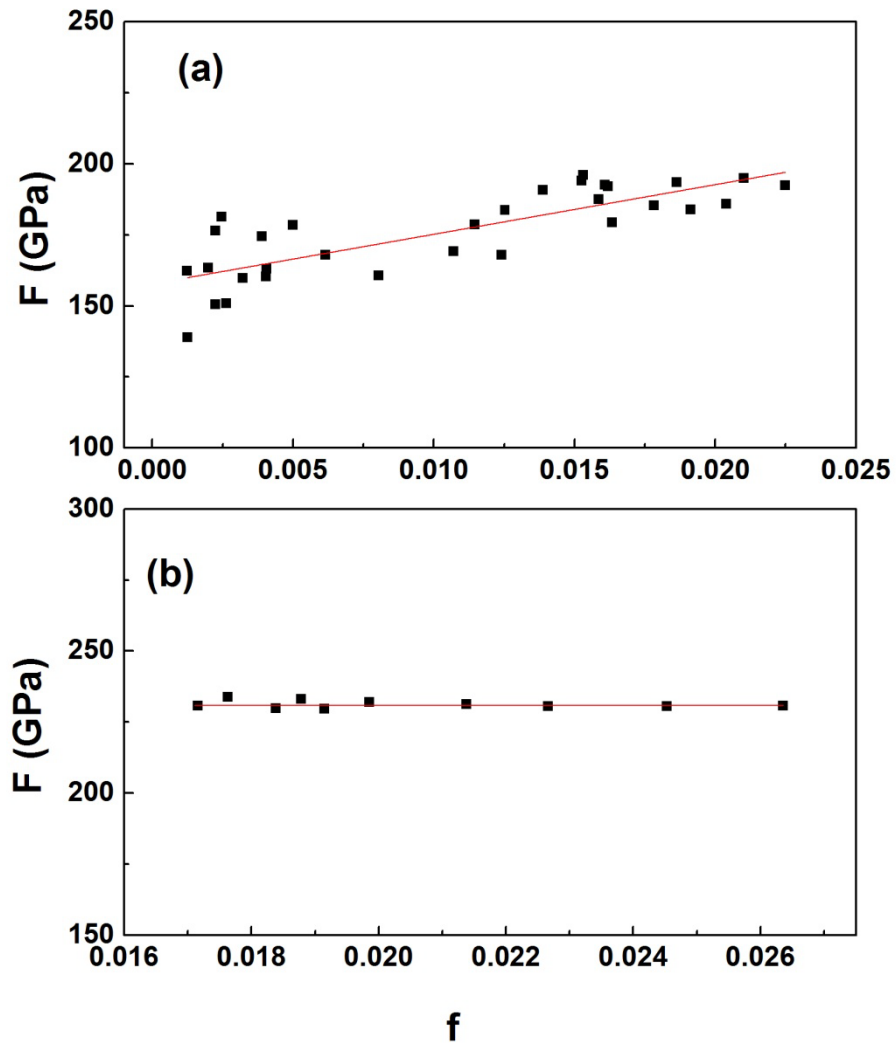
Figure 3: (Colour online) Rietveld refined diffraction patterns (a) wolframite phase at 1.2 GPa (b) HP wolframite phase at 20.7 GPa (c) recovered wolframite phase at 0.1GPa. Symbol denotes the experimental data points and solid line denotes the calculated profile. Background and residual plots are also plotted. Ticks indicate the calculated positions of the Bragg peaks. In (a) upper and lower vertical tick marks are for wolframite sample and pressure calibrant respectively. In (b) upper ticks are for the LP phase (minor contribution) and the bottom most are for the HP phase (major phase). Third and second tick marks from the bottom are for sample chamber and pressure calibrant respectively. In (c) Recovered wolframite phase at 0.1 GPa.
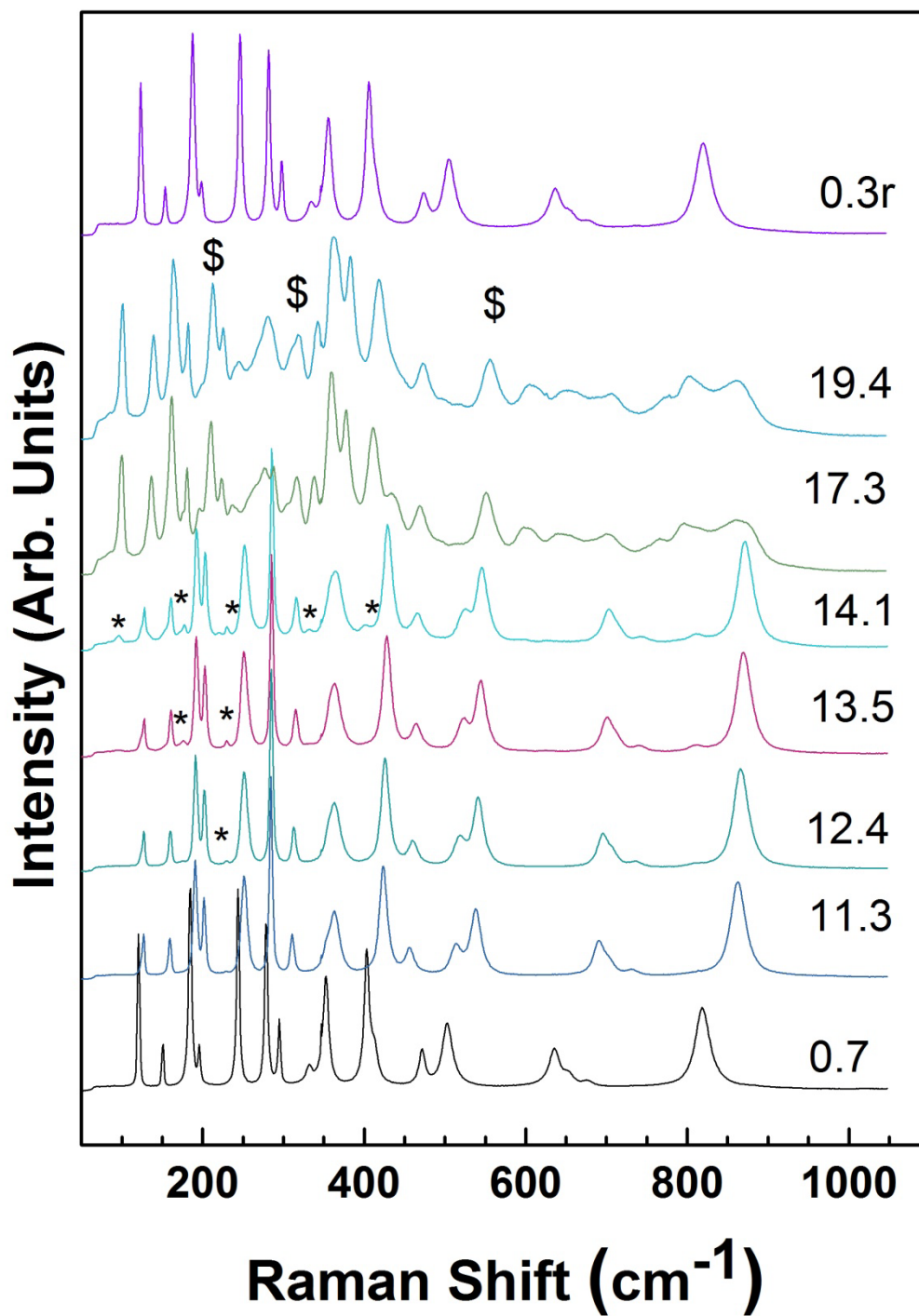
Figure 4: Pressure dependence of unit-cell parameters extracted from the Rietveld refinement of the XRD data and from first principles calculations for both LP and HP phases of InNbO$_4$. Solid square and circle denotes the data for low pressure and high pressure phase respectively. Solid lines denote the data from theory. Inset shows the pressure variation of monoclinic angle β in LP and HP phases.
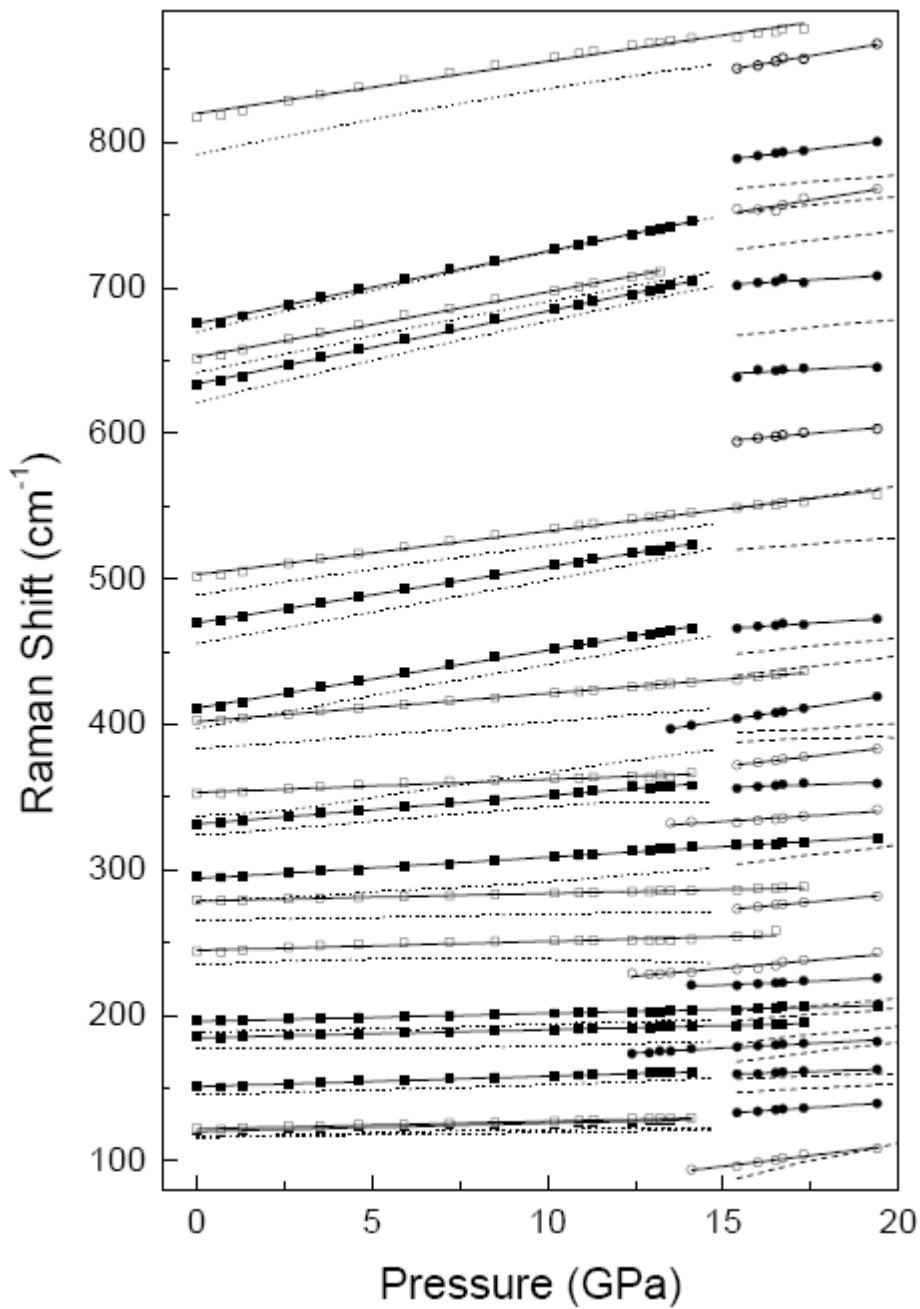
Figure 5: Pressure volume data for LP and HP phases from experiments and calculations. Solid square and circle represents the experimental data points for LP and HP phases. Solid lines are the data from theory. Dashed (-----) and dotted (·······) lines are the 2nd and 3rd order BM-EOS fit to LP and HP experimental data respectively.

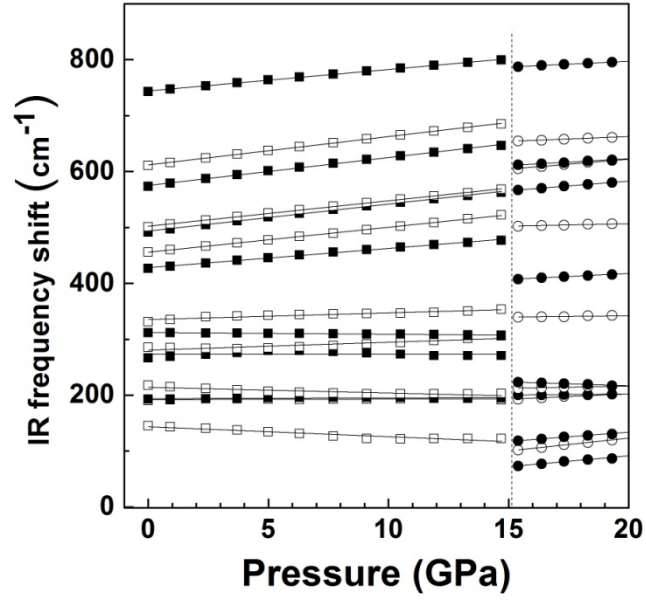**Figure 6**: f-F (Eulerian strain vs. normalized stress) plot for low and high pressure phases.

Symbols are experimental points and solid line is linear fit to the data.

Figure 7: Selection of Raman spectra measured at different pressures (indicated in the plot). The asterisks indicate the peaks from HP phase when this is the minority phase. The dollar symbols indicate the detection of peaks of the low-pressure phase when this is the minority phase. (r) denotes a spectrum measured upon decompression.
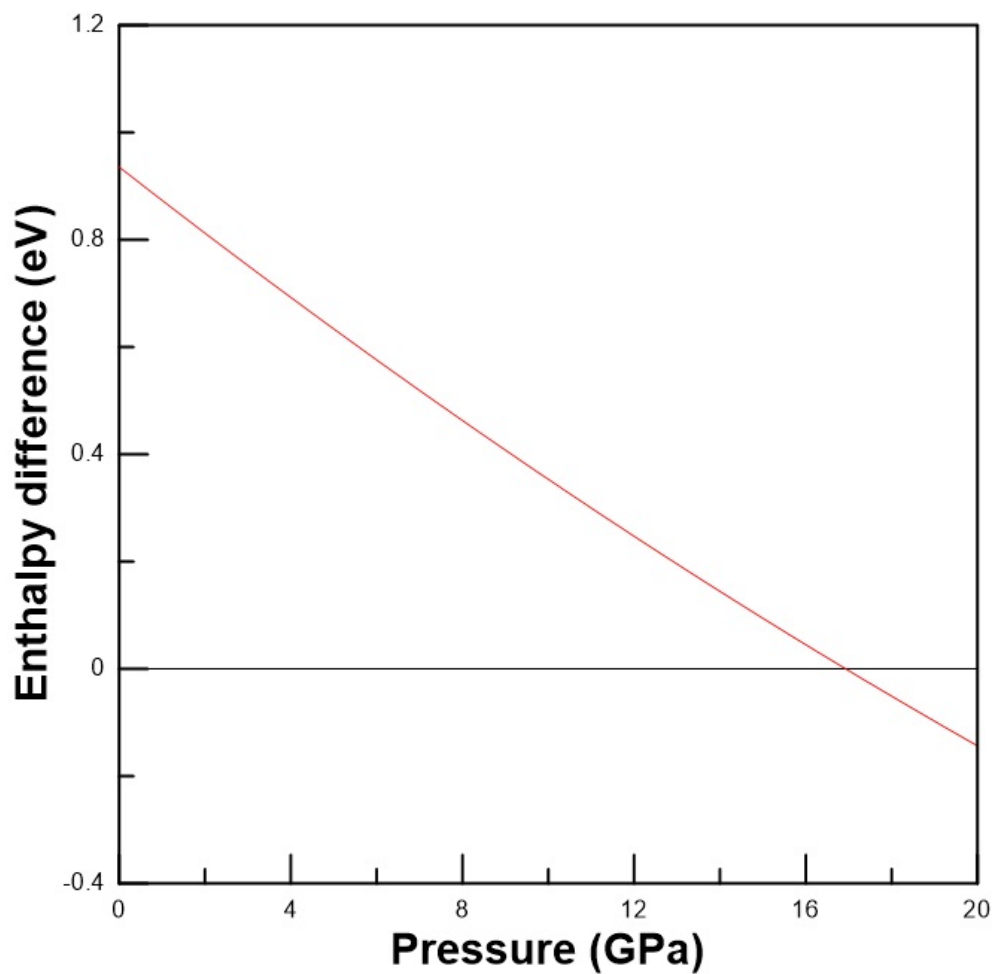
Figure 8: Pressure dependence of Raman modes of low-pressure (squares) and high-pressure (circles) phases. Solid and empty symbols are used alternatively to facilitate the identification of different modes. The solid lines are the results of linear fits shown in Tables III and IV. Dotted and dashed lines represent the calculated phonon frequencies of LP and HP phases.
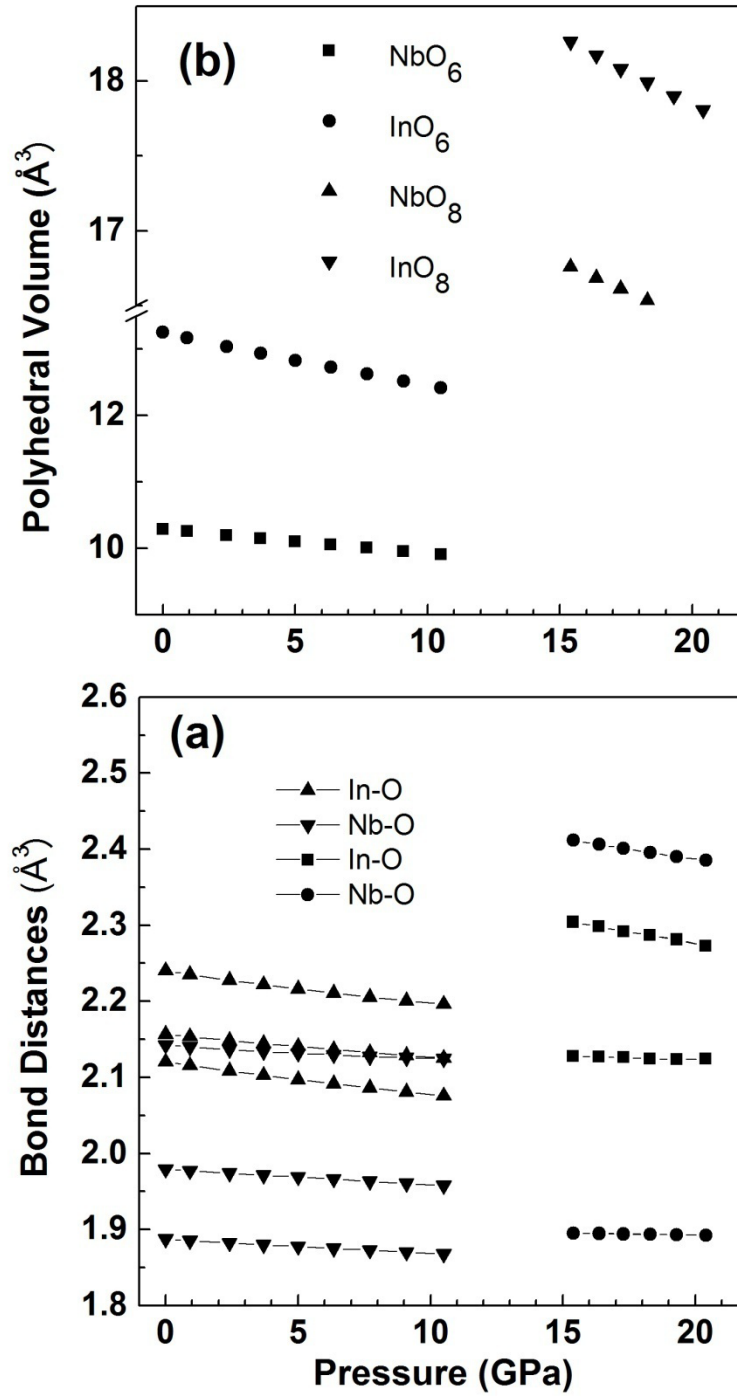
Figure 9: Pressure dependence of IR modes of low-pressure (squares) and high-pressure (circles) phases of InNbO₄. Solid and empty symbols are used alternatively to facilitate the identification of different modes. The solid lines are the results of linear fits shown in Table V

Figure 10: Calculated enthalpy difference as function of pressure showing the phase transition. The ambient-pressure wolframite phase has been taken as a reference (horizontal black line) and the HP phase is represented with the red line.

Figure 11 (a): Pressure variation of various bond lengths of In and Nb cation with oxygen anion in LP and HP phases of InNbO4 (b) octahedral and dodecahedral volume of In and Nb in LP and HP phases of InNbO4 obtained from theory.

Figure Captions

Figure 1: (color online) Crystal structure of low-pressure wolframite (top) and high-pressure wolframite (bottom) phases of $InNbO_4$. Octhahedral and dodecahedral coordination around In and Nb cations are clearly seen in LP and HP phase respectively.

Figure 2: (color online) Pressure evolution of x-ray diffraction patterns of $InNbO_4$. Pressures in GPa, are indicated on the right hand side y-axis. The asterisks denote the peaks from cu pressure marker whereas # indicates the peaks from w sample chamber. The intense peaks from the ambient wolframite structure have been marked. Arrows indicate the appearance of new diffraction peaks from the high pressure phase. Data marked with r were measured during pressure unloading.

Figure 3: (Colour online) Rietveld refined diffraction patterns (a) wolframite phase at 1.2 GPa (b) HP wolframite phase at 20.7 GPa (c) recovered wolframite phase at 0.1GPa. Symbol denotes the experimental data points and solid line denotes the calculated profile. Background and residual plots are also plotted. Ticks indicate the calculated positions of the Bragg peaks. In (a) upper and lower vertical tick marks are for wolframite sample and pressure calibrant respectively. In (b) upper ticks are for the LP phase (minor contribution) and the bottom most are for the HP phase (major phase). Third and second tick marks from the bottom are for sample chamber and pressure calibrant respectively. In (c) Recovered wolframite phase at 0.1 GPa.

Figure 4: Pressure dependence of unit-cell parameters extracted from the Rietveld refinement of the XRD data and from first principles calculations for both LP and HP phases of $InNbO_4$. Solid square and circle denotes the data for low pressure and high pressure phase respectively. Solid lines denote the data from theory. Inset shows the pressure variation of monoclinic angle β in LP and HP phases.

Figure 5: Pressure volume data for LP and HP phases from experiments and calculations. Solid square and circle represents the experimental data points for LP and HP phases. Solid lines are the data from theory. Dashed (-----) and dotted (·······) lines are the 2nd and 3rd order BM-EOS fit to LP and HP experimental data respectively.

Figure 6: f-F (Eulerian strain vs. normalized stress) plot for low and high pressure phases. Symbols are experimental points and solid line is linear fit to the data.

Figure 7: Selection of Raman spectra measured at different pressures (indicated in the plot). The asterisks indicate the peaks from HP phase when this is the minority phase. The dollar symbols indicate the detection of peaks of the low-pressure phase when this is the minority phase. (r) denotes a spectrum measured upon decompression.

Figure 8: Pressure dependence of Raman modes of low-pressure (squares) and high-pressure (circles) phases. Solid and empty symbols are used alternatively to facilitate the identification of different modes. The solid lines are the results of linear fits shown in Tables III and IV. Dotted and dashed lines represent the calculated phonon frequencies of LP and HP phases.

Figure 9: Pressure dependence of IR modes of low-pressure (squares) and high-pressure (circles) phases of InNbO$_4$. Solid and empty symbols are used alternatively to facilitate the identification of different modes. The solid lines are the results of linear fits shown in Table V.

Figure 10: Calculated enthalpy difference as function of pressure showing the phase transition. The ambient-pressure wolframite phase has been taken as a reference (horizontal black line) and the HP phase is represented with the red line.

Figure 11 (a): Pressure variation of various bond lengths of In and Nb cation with oxygen anion in LP and HP phases of InNbO$_4$ (b) octahedral and dodecahedral volume of In and Nb in LP and HP phases of InNbO$_4$ obtained from theory.

Table Captions

Table 1: Structural parameters of LP wolframite InNbO$_4$ at 1.2 GPa (Top), and HP wolframite at 20.7 GPa. Both structures can be described with space group *P2/c*. For the LP(HP) phase, the goodness of fit parameters are: R$_{wp}$=1.43 % and R$_P$=1.2 % (R$_{wp}$=1.1 % and R$_P$=1.0 %). The Wyckoff position for each atom is indicated in the first column. For the HP phase only the In and Nb positions have been refined.

Table 2: EOS parameters for different structures determined from present experiments and calculations.

Table 3: Measured and calculated Raman modes at ambient pressure, pressure coefficients, and Grüneisen parameters for the low-pressure phase of InNbO$_4$. R$_\omega$ is the relative difference between measured and calculated frequencies.

Table 4: Measured and calculated Raman modes, pressure coefficients, and Grüneisen parameters of high pressure phase of InNbO4 at 19.4 GPa. R$_\omega$ is the relative difference between measured and calculated frequencies.

Table 5: Calculated IR modes and pressure coefficients for the low- and high-pressure phases of InNbO$_4$, at ambient pressure and 20.5 GPa, respectively.

Table 6: Structural details of wolframite from calculations for InNbO$_4$ at ambient pressure (top), high pressure (bottom) at 20.4 GPa